High-Speed Silicon Modulator With Slow-Wave Electrodes and Fully Independent Differential Drive

Ran Ding, Yang Liu, Yangjin Ma, Yisu Yang, Qi Li, Andy Eu-Jin Lim, Guo-Qiang Lo, *Member, IEEE*, Keren Bergman, *Fellow, IEEE*, Tom Baehr-Jones, and Michael Hochberg

***Abstract*—We demonstrate a fully independent differential-drive capable of traveling-wave modulator in silicon using slow-wave transmission line electrode. The reported 3.5-mm device achieves a bandwidth of 27 GHz at −1 V bias with 7.8-V small signal V_π and 50-Ω impedance. Raising the impedance to this extent requires effectively expanding the RF mode size and radically changes the RF phase velocity, but we show that this can be done with minimal crosstalk effects between the two arms and overall velocity mismatch, and thus, with a high EO bandwidth achieved. 40-Gb/s operation is demonstrated with 1.6-V_{pp} differential-drive, and performance comparisons to Lithium Niobate modulators are made.**

***Index Terms*—Integrated optics devices, integrated optoelectronic circuits, modulators.**

I. Introduction

HIGH-SPEED modulators are key building blocks in silicon photonics [1]. Traveling-wave Mach–Zehnder (TWMZ) modulators are often deployed in practical systems [2] because they offer several key properties, such as thermal insensitivity and high robustness against fabrication variations. Proper RF design is critical to achieve good performance on TWMZ devices. With typical silicon p-n junctions and waveguide geometries of the phase shifter, 50 Ω device impedance is usually challenging to achieve due to the high junction capacitance per unit length; instead, TWMZ is often implemented at lower impedances (near 30 Ω for instance) [3]–[6]. In addition to creating reflections to driving circuitries, low device impedance incurs bandwidth penalty when terminated with standard 50 Ω impedance [7], [8]. This design difficulty is worsened when the modulator designs employ more advanced p-n junctions that offer improved $V_\pi L$ but often at the cost of high capacitance [9], [10]. Another key aspect of the RF design is the RF cross-talk effect in multi-conductor TWMZ devices due to the excitation and coupling of multiple RF modes, as has been discussed by [4] and [11] in particular. It is indeed a bandwidth-limiting effect as evidenced by the dips in the EO or RF S21 in several results [4]–[6], [12]–[14].

In this paper we demonstrate a differential-drive TWMZ modulator using slow-wave electrodes. The slow-wave electrode design significantly increases the achievable inductance per unit length, thus effectively raise the device impedance. The core aspect of a slow-wave TWMZ design is pulling the current paths farther apart laterally from each other in order to raise the transmission line inductance. This raises device impedance, but can potentially raise ohmic losses as well as expanding the size of the RF mode. In particular, the expanded RF mode then more readily exhibits long-range interference, and directional coupling between the two arms, leading to potentially destructive cross-talk within the modulator.

Slow-wave electrode designs have been used in III-V compound modulators [15], [16], though in these cases were used primarily to achieve velocity matching between RF and optical wave. In the silicon system, this type of design has only been explored by Merget *et al.* [11] and Chen *et al.* [17]. In [17], the modulator uses a single-drive push-pull configuration. The back-to-back p-n junction configuration reduces capacitance loading in half but also reduces the voltage dropped on each arm by the same factor, therefore this configuration incurs higher drive voltage compared to differential-drive. In [11], the GSSG structure supports three RF modes. The authors addressed the cross-talk challenge by utilizing a RF common-mode drive configuration in which only one RF mode was selectively excited.

Our device operates with a GSGSG configuration, as shown in Fig. 3. The design ensures true single-RF mode operation by laterally connecting ground traces together using lower level metal layer (Metal1), and the single-RF mode operation is verified experimentally by differential mode and single-ended mode S-parameter measurement. The RF loss associated with slow-wave electrode is maintained to be a small portion compared to the overall RF loss of the device and therefore is not a limiting factor of device bandwidth. A large *G* patch in the center of the device enables isolation between the two arms to be achieved,

Manuscript received February 18, 2014; revised May 12, 2014; accepted May 12, 2014. Date of publication May 20, 2014; date of current version May 30, 2014. This work was supported by the AFOSR STTR Grants FA9550-12-C-0079 and FA9550-12-C-0038, as well as an National Research Foudation Fellowship NRF2012NRF-NRFF001-143 , the Presidential Early Career Award in Science and Engineering (FA9550-13-1-0027) and ongoing funding for OpSIS (FA9550-10-1-0439), and Portage Bay Photonics, LLC.

R. Ding, Y. Liu, Y. Ma, Y. Yang, and T. Baehr-Jones are with the Department of Electrical and Computer Engineering, University of Delaware, Newark DE 19716 USA (e-mail: dingran@udel.edu; phyliuyang@gmail.com; mayj@udel.edu; yangyisu@udel.edu; baehrjt@udel.edu).

Q. Li, K. Bergman are with the Department of Electrical Engineering, Columbia University, New York NY 10027 USA (e-mail: ql2163@columbia.edu; bergman@ee.columbia.edu).

A. E.-J. Lim and G.-Q. Lo are with the Institute of Microelectronics, Agency for Science, Technology and Research, 138632 Singapore (e-mail: limej@ime.a-star.edu.sg; logq@ime.a-star.edu.sg).

M. Hochberg is with the Department of Electrical and Computer Engineering, University of Delaware, Newark DE 19716 USA, the Department of Electrical and Computer Engineering, University of Singapore, 119088 Singapore, and also with the Institute of Microelectronics, Agency for Science, Technology and Research, 138632 Singapore (e-mail: hochberg@udel.edu).

Color versions of one or more of the figures in this paper are available online at http://ieeexplore.ieee.org.

Digital Object Identifier 10.1109/JLT.2014.2323954

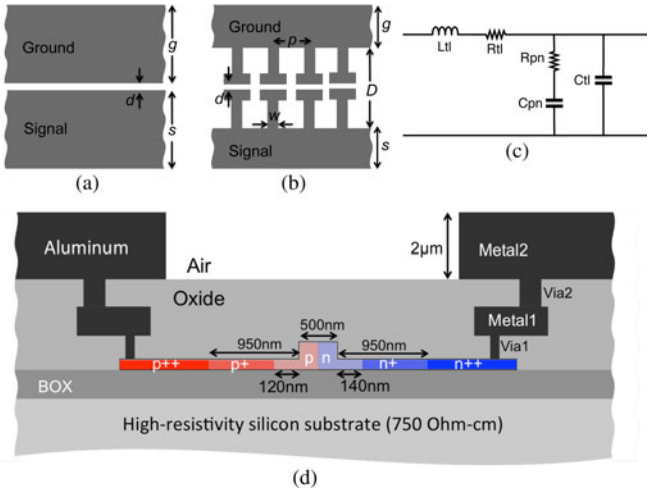

Fig. 1. (a) Coplanar strip transmission line. (b) Slow-wave transmission line. (c) Simplified equivalent circuit model of p-n junction loaded transmission line electrode. (d) Simplified cross sectional diagram of the phase shifter, not to scale.

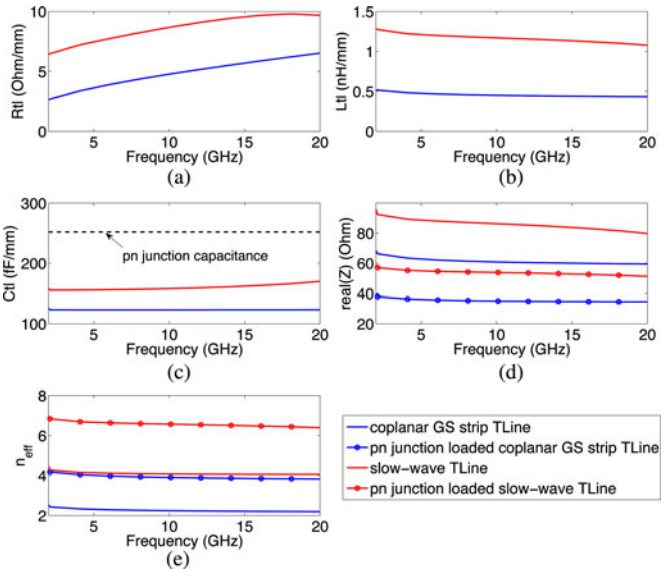

Fig. 2. Comparison of simulated transmission line parameters. Coplanar GS strip line parameters: $g = 50\mu$m, $s = 50\mu$m, and $d = 5\mu$m. Slow-wave transmission line parameters: $g = 30\mu$m, $s = 10\mu$m, $d = 6\mu$m, $w = 5\mu$m, $p = 14\mu$m and $D = 100\mu$m.

which allows for completely independent drive of both arms. This is compatible with commonly used differential signaling scheme and is potentially useful for advanced modulation formats such as quadrature-phase-shift-keying (QPSK).

Due to the combination of large inductance and capacitance per unit length, the RF effective index is 6–7 in the device we report. It is significantly larger than in a typical coplanar strip transmission line designs, where the loaded device RF index is close to the optical group index (3.5–4). We analyze the effect of using periodical phase matching and experimentally demonstrate that using this technique the achieved bandwidth is within a few percent of a continuously velocity-matched modulator.

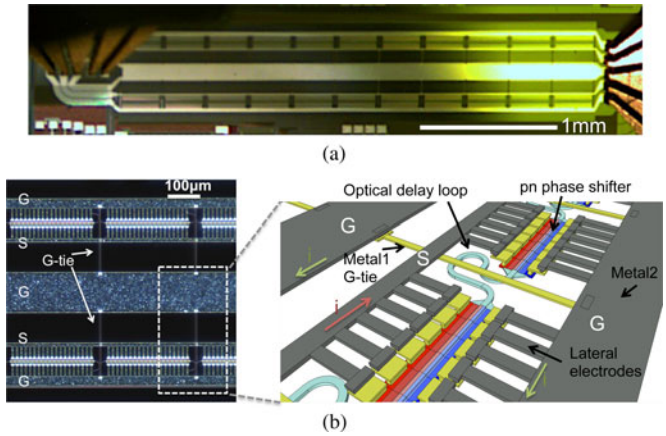

Fig. 3. (a) Fabricated device under probed testing: GSGSG probe on the right is for driving, and GSGSG probe on the left is for providing 50-Ω termination to each device arm, and (b) microphotograph of a section of the device, mainly top metal (Metal2) is visible. Inset (not-to-scale): details near a ground-plane lateral connection (*G*-tie) and the optical delay loop for re-aligning optical and RF phase.

The 3.5-mm device we report shows an EO 3-dB bandwidth of 21.5 GHz at 0 V bias and 27 GHz at -1 V bias. Both numbers match closely to RF S21 6.4-dB bandwidths, suggesting little RF reflection, cross-talk or other detrimental RF effects are occurring [18]. The RF reflection (S11) is better than -18 dB within the 3-dB bandwidth under both bias voltages. 5.5 V voltage on each arm differentially achieves a π phase shift (i.e. full extinction). Between -1 and 0 V the small-signal V_π is 7.8 V, which is useful metric to estimate phase shift and extinction at low drive voltages. 40 Gb/s error-free operation is demonstrated with a power-efficient 1.6 V_{pp} differential-drive. When driving the device with 4.8 V_{pp} differential-drive, the bit-error-rate (BER) versus optical signal-to-noise ratio (OSNR) performance is comparable to that of a commercial 40-Gb/s Lithium Niobate modulator (single-drive) with similar driving voltage amplitude. This establishes that the level of nonlinear distortion found within our silicon TWMZ is minimal and should not be an issue for utilization in communications systems.

II. Device Design and Fabrication

A. Slow-Wave Transmission Line Electrode

Slow-wave transmission line electrode [15], [16] refers to ground-signal (GS) or ground-signal-ground coplanar strip transmission lines loaded with periodic segmented lateral electrodes [see Fig. 1(a)–(b)]. The segmented lateral electrodes in slow-wave transmission line restrict RF currents to flow only in the continuous G and S strips that have much larger separation (D) thus providing higher inductance per unit length (L_{tl}). To build a traveling-wave modulator, sections of capacitive p-n junction phase shifters are loaded in the gap d [see Fig. 1(b)]. Fig. 1(c) shows the distributed circuit model [19]: L_{tl}, R_{tl} and C_{tl} are the unit length inductance, resistance and capacitance respectively of the metal transmission line. C_{pn} and R_{pn} are the p-n junction capacitance and series resistance (from the *G* and *S* traces to the p-n junction) respectively.

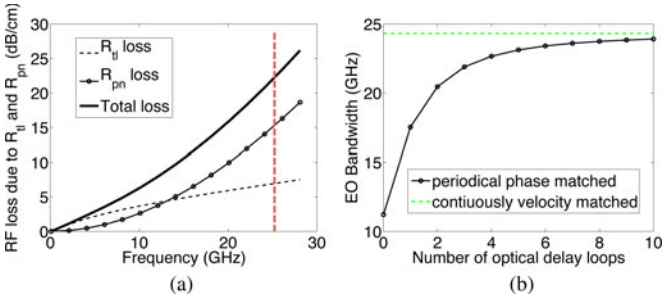

Fig. 4. (a) Simulated RF loss due to p-n junction series resistance R_{pn} and transmission line metal resistance R_{tl}, red dashed line marks the 3-dB bandwidth location, and (b) Simulated EO bandwidth versus numbers of optical delay loops, the green dashed line marks the 3-dB bandwidth of a continuously velocity matched modulator that has the same RF loss.

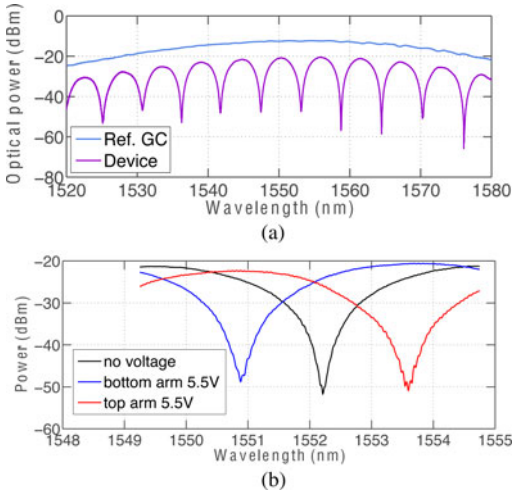

Fig. 5. (a) Optical spectra: device versus reference grating coupler (GC). (b) π phase shift under 5.5 V voltage on each arm.

Fig. 1(d) illustrates the cross-section of the p-n junction phase shifter used in our device with key dimensions annotated. The device was fabricated at the Institute of Microelectronics, A*STAR, Singapore, through an OpSIS multi-project-wafer run [20]. The fabrication process enables monolithic integration of both modulators and photodetectors [21], therefore it is straightforward to incorporate the designed modulator in building larger systems. The phase shifter uses striploaded ridge waveguide with a slab thickness of 90 nm and ridge height of 220 nm. The p-n junction is formed at the center of the waveguide by $5 \times 10^{17}/\mathrm{cm}^3$ p-dopants and $3 \times 10^{17}/\mathrm{cm}^3$ *n*-dopants. The intermediate *p*+ and *n*+ dopants are on the level of $2 \times 10^{18}/\mathrm{cm}^3$. They significantly decrease the series resistance R_{pn} while maintaining low optical loss [6]. The junction capacitance C_{pn} is approximately 250 fF/mm at 0 V bias and the series resistance R_{pn} is 0.7 Ω·cm. We use the top metal layer Metal2 for the *G* and *S* traces as well as the segmented lateral electrode. This metal layer is thicker and mostly on top of the oxide layer thus offers a lower resistance and lower capacitance. The lower level metal Metal1 is used for local connections to silicon.

B. Comparison to Coplanar Strip Transmission Line

To illustrate the key differences in RF characteristics between coplanar strip transmission lines and slow-wave transmission lines, we show the numerical analysis of a design case of each. Coplanar strip transmission lines have been frequently used to build traveling-wave modulators in silicon. We analyze the RF design used in [6], with ground trace width $g = 50$ μm, signal trace width $s = 50$ μm and GS gap $d = 5$ μm.

For slow-wave transmission line, we analyze the RF design used in the modulator that we report here. Its geometric parameters are labeled in Fig. 1(b): ground trace width $g = 30$ μm, signal trace width $s = 10$ μm, GS gap $d = 6$ μm, GS trace separation $D = 100$ μm, lateral electrode period $p = 14$ μm, and lateral electrode width $w = 5$ μm. In addition to the structure shown in Fig. 1(b), the actual modulator device has an additional center *G* patch to isolate the two device arms (see Fig. 3), this *G* patch is included in the simulation.

We used Ansoft HFSS for 3-D electromagnetism simulation and extracted the RF line parameters (R_{tl}, L_{tl} and C_{tl}) as shown in Fig. 2. We further combine them with the junction parameters C_{pn} and R_{pn} to calculate the loaded line RF effective index n_{eff} and impedance Z, also shown in Fig. 2. As it is evident from Fig. 2, compared to the coplanar strip transmission line with similar GS gap d, the slow-wave transmission line offers much higher (2.5×) inductance per unit length while only have 25% more capacitance, therefore effectively raises the device RF impedance.

C. Device Configuration and Design Considerations

The fabricated Mach–Zehnder modulator with slow-wave electrode is shown in Fig. 3. We include a wide center ground patch to isolate the two device arms. Both signal traces are connected to the cathode of the p-n junction on each arm of the modulator, thus differential electrical signaling generates differential phase on the device arms. GSGSG probes, visible in the micrograph, were used for driving and providing 50 Ω termination to the device in high-speed testing. In such a multi-conductor structure, multiple RF modes exist: the desirable RF mode exists between the *S* and side *G* trace that are directly connected to the p-n junction phase shifter; in addition, the center *G* patch and the *S* traces also support so-called "slot-line" mode. One way of suppressing cross-talk to and excitation of such unwanted modes is through wire bond air bridges [22]. In our device, we implemented such lateral ground connections (namely *G*-tie) in lower level metal (Metal1), as illustrated in Fig. 3(b). We chose a device length of 3.5 mm, of which 3-mm length is loaded with p-n junction phase shifters. The overall device width is 620 μm. Simulation result suggests that at 0 V bias on the p-n junction the device RF loss reaches 6.4 dB near 24 GHz, indicating the EO bandwidth could reach this number. The periodicity of *G*-tie is approximately 300 μm. The device in total has 12 *G*-tie regions.

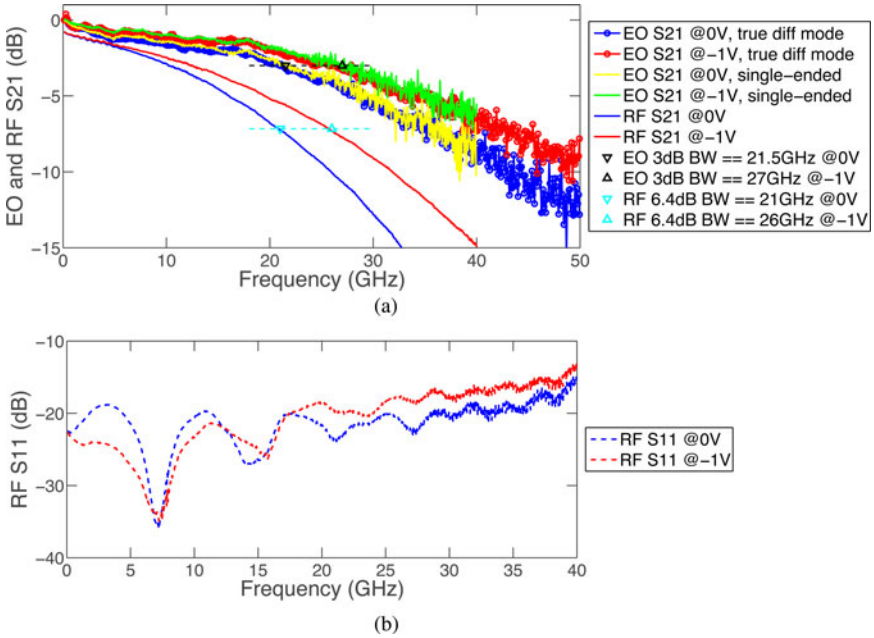

Fig. 6. EO and RF S-parameters at 0 and −1 V bias. (a) EO and RF S21. (b) RF S11.

In the previous section we compared the RF characteristics of a coplanar strip transmission line and a slow-wave transmission line. Besides the desirable increase in inductance and achievable device impedance, there are two aspects in slow-wave transmission line that are worth careful considerations.

The first one is the higher R_{tl}. Fortunately, the RF loss due to the metal conductor resistance R_{tl} scales with respect to $\sqrt{f}$, whereas the RF loss due to the silicon resistance R_{pn} scales with respect to f^2 [19]. Using the RF parameters from HFSS simulation and equation (6) in [19], we show that in our device near the 3-dB bandwidth R_{tl} loss is only 30% of the total RF loss, as presented in Fig. 4(a). Therefore, even though the slow-wave transmission line exhibits higher R_{tl} induced RF loss, it is still far from a limiting factor for device EO bandwidth—RF loss due to R_{pn} remains to be the dominating loss mechanism at high frequency.

The other consideration is that n_{eff} in the slow-wave electrode device is close to 6.5 (see Fig. 2), which is substantially higher than the optical group index [23] in the silicon waveguide (approximately 3.8). To address the strong velocity mismatch between RF and optical waves, we break down the whole device into sections and include an optical delay loop after each section to compensate for the faster optical wave, fully realigning its phase to the RF wavefront. To calculate the device bandwidth with respect to different numbers of optical delay loops (i.e. numbers of sections) while maintaining the total device length constant, we use the RF loss in Fig. 4(a) and the RF and optical indices mentioned above to carried numerical simulations. We further assume RF reflection is negligible and each optical delay loop correctly compensates the phase walk-off in the section of traveling-wave phase-shifter that precedes it. According to the simulation result shown in Fig. 4(b), we divided the device into 11 sections and implemented ten optical delay loops such that the device bandwidth is within 2% of a continuously perfectly velocity match modulator. The optical delay loops are implemented in the *G*-tie regions that do not have p-n junction loading to reuse space, as illustrated in Fig. 3(b).

III. Measurement and Discussion

A. Optical Spectra and DC V_π

The device uses grating couplers (GCs) to couple light on and off the chip. Routing waveguide of a few millimeter length is used to connect the device input and output to the GCs. To extract the device insertion loss we measured the optical spectra of the device and a reference GC loop near the device, as shown Fig. 5(a). The fringes in the device spectrum are due to 100 μm intentional imbalance of the Mach–Zehnder arm lengths. This allows convenient change of the modulator phase bias by tuning the wavelength. In actual systems, balanced devices should be used and the phase imbalance between the two arms can be controlled through thermal tuning [6].

The total on-chip insertion loss of the device is measured to be 8.0 dB. According to further measurements of each component, this insertion loss includes the following: 0.3 dB due to routing waveguide between the device itself and the input and output GCs, 0.9 dB due to the two Y-junctions, 3.6 dB due to the 3-mm active phase shifter (with implantation design tradeoff discussed in [24]), the remaining 3.2 dB is due to two layout issues in the G-tie regions: (1) the Metal1 G-tie accidentally overlapped with a long section of waveguide and 2) too abrupt waveguide tapers were used between the optical delay loops and the striploaded phase shifters. This 3.2 dB loss can be substantially reduced by (1) switching to Metal2 for the part of G-tie that covers the waveguide and (2) using striploaded waveguide in the optical delay loops thus avoid tapers all together. As shown in [25],

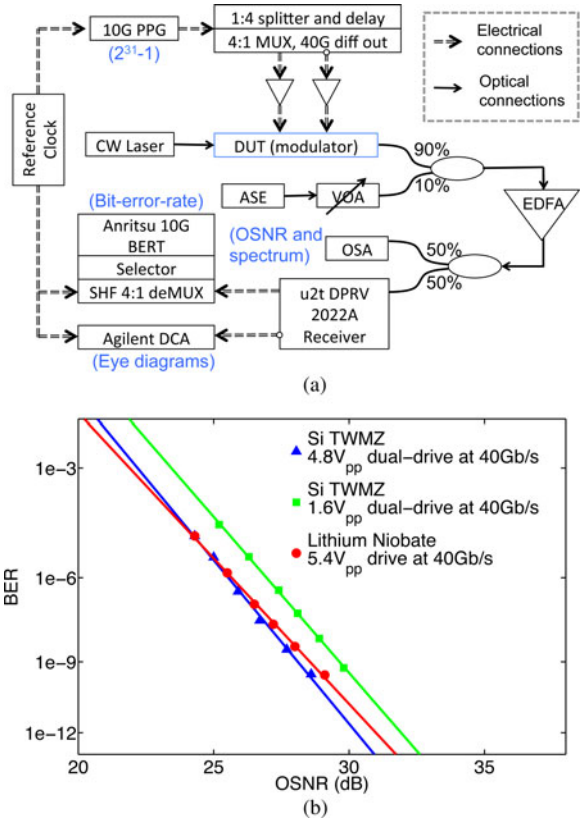

Fig. 7. (a) Experiment setup for BER and eye-diagram measurements (PPG: pulse pattern generator, OSA: optical spectrum analyzer, VOA: variable optical attenuator, ASE: amplified spontaneous emission). (b) BER versus OSNR.

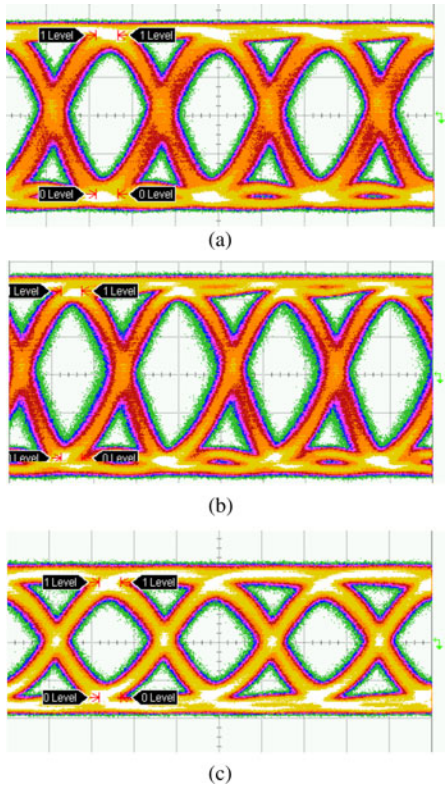

Fig. 8. Error-free (BER $<$ 1e-12) 40 Gb/s eye diagrams taken during the BER measurement: (a) Lithium Niobate modulator under 5.4 V_{pp} drive. (b) Si TWMZ modulator under 4.8 V_{pp} differential drive. (c) Si TWMZ modulator under 1.6 V_{pp} differential drive.

striploaded waveguide can still maintain a similarly compact bend radius. We then measured phase shift versus voltage on both arms. Between -1 and 0 V the small-signal V_π is on average 7.8 V. A full π phase shift is achieved with 5.5 V voltage differential drive, as shown in Fig. 5(b).

B. Small-Signal EO Bandwidth

We then characterized the small-signal EO bandwidth of the device through S-parameter measurements using a vector-network-analyzer (VNA) and a 70-GHz bandwidth photodetector from u2t. The measurements were carried out using the probing configuration shown in Fig. 3(a), where a GSGSG probe was used for driving and another GSGSG probe (with termination resistors connected) was used for providing 50 Ω termination to each device arm.

First, "single-ended" EO *S*-parameter measurement was carried out using an Agilent E8361C 2-port VNA. In this experiment one arm was driven and the unused arm was terminated with 50 Ω at both ends. The result is shown in Fig. 6(a) in yellow and green, for 0 and -1 V bias respectively. Secondly, we repeated the EO *S*-parameter measurement using true differential-mode excitation with an Agilent N5227A 4-port VNA, in which the two device arms were driven by the VNA differentially. The corresponding result is shown in Fig. 6(a) in blue and red dotted lines that almost completely overlap with the single-ended measurements. These two sets of EO bandwidth measurements suggest that the device bandwidth is 21.5 GHz at 0 V bias and 27 GHz at -1 V bias. The smoothness of the EO S21 and the similarity between single-ended and differential-mode S21 suggest that *G*-tie is effective in suppressing RF cross-talk and multi-mode effects, and the two device arms are fully independent. This enables the device to be compatible with single-ended and differential driving scheme, which are the most commonly used in driving circuitries. Having two fully-independent arms is also potentially useful for advanced modulation format such as QPSK, where the two device arms carry uncorrelated data patterns.

We further carried out calibrated RF *S*-parameter measurement, in which the termination probe was connected to a VNA port to receive the RF "through" signal at the end of the device. This experiment was taken on each individual arm, with the unused arm terminated by 50 Ω. The measured RF S21 and S11 are shown in Fig. 6 for a direct comparison to the EO S21. We observed a 6.4-dB bandwidth of 21 GHz at 0 V bias and 26 GHz at -1 V bias. The importance of RF 6.4-dB bandwidth is that if device EO bandwidth is only limited by RF attenuation, EO 3-dB bandwidth should coincide with RF 6.4-dB bandwidth [7], [18].This is indeed the case as suggested by the EO S21. Thus overall RF and optical velocities are indeed closely matched and other detrimental RF effects such as strong RF reflections or RF cross-talk effects do not exist in the device. The extracted RF

index of the loaded slow-wave electrode is 6.1 near 25 GHz at 0 V bias, only a small deviation from the simulated value 6.5. We note that the measured RF 6.4-dB bandwidth at 0 V bias is 21 GHz, slightly lower than the simulated value 24 GHz (see Section II-C.). This is attributed to the high metal-to-silicon contact resistance on *p*++ silicon, which was measured in separate test structures to be 5–10 $\mathrm{k}\Omega{\cdot}\mu\mathrm{m}^2$ depending on via sizes. This corresponds to a 0.1–0.2 $\Omega\cdot$ cm increase in R_{pn} that explains this slight bandwidth degradation.

C. Data Transmission Measurements

EO *S*-parameters characterize device bandwidth in small-signal regime and provide useful information validating device design and modeling accuracy. The large-signal dynamic performance of the device in actual high-speed data transmission was evaluated by BER versus OSNR measurement described in this section. The experiment setup is shown in Fig. 7(a). Non-return-to-zero pseudo-random-bit-stream with $2^{31}-1$ pattern at 10 Gb/s was generated by an Anritsu pulse pattern generator (PPG) and then four-way split and delayed before being multiplexed into a 40 Gb/s using an SHF 24210A module. The differential 40 Gb/s output was amplified by a pair of Centellax OA4MVM3 driver amplifiers, then attenuated to the desired amplitude by passive attenuators. The pair of driving signal was applied to the device through a pair of high-speed bias-tee and a 65 GHz GSGSG probe. The device probing and termination configuration were the same as in the *S*-parameter measurements. A tunable laser was used as the input light to the device and its wavelength was chosen to set the device near quadrature (-3 dB point). The modulated light was combined with tunable amplified spontaneous emission (ASE) noise loading that varied the OSNR in the experiments and then passed through an erbium-doped fiber amplifier (EDFA). The output optical signal was split into two branches and fed into an optical spectrum analyzer (OSA) for OSNR monitoring and a u2t DPRV 2022A receiver (ac coupled, -10 dBm sensitivity) with differential outputs. During the experiments the optical modulation amplitude into the receiver was maintained to be near 0 dBm, well above its sensitivity. One of the receiver output was connected to an Agilent 86100B digital communication analyzer (DCA) for eye-diagram viewing. The other output was connected to an SHF 34210A 1:4 demultiplexer followed by an SHF 58210A selector. The demultiplexed and selected tributary was sent to an Anritsu MU181040A error-detector for BER test. The reported BER is an average from all four tributaries.

We carried out the BER versus OSNR measurement on the silicon TWMZ modulator and a commercial Lithium Niobate 40-Gb/s modulator that has 5.9 V_{π} for comparison. The Lithium Niobate modulator is a single-drive component and is driven with 5.4 V_{pp}, which was the maximal available drive voltage from the driver amplifier due to limited output voltage from the multiplexer. The silicon TWMZ modulator was tested with two different driving configurations: 4.8 V_{pp} drive on each arm with 3 V reverse bias and 1.6 V_{pp} drive on each arm with 1.5 V reverse bias. Because the receiver is ac coupled, an extinction ratio (ER) measurement was not readily available on the DCA.

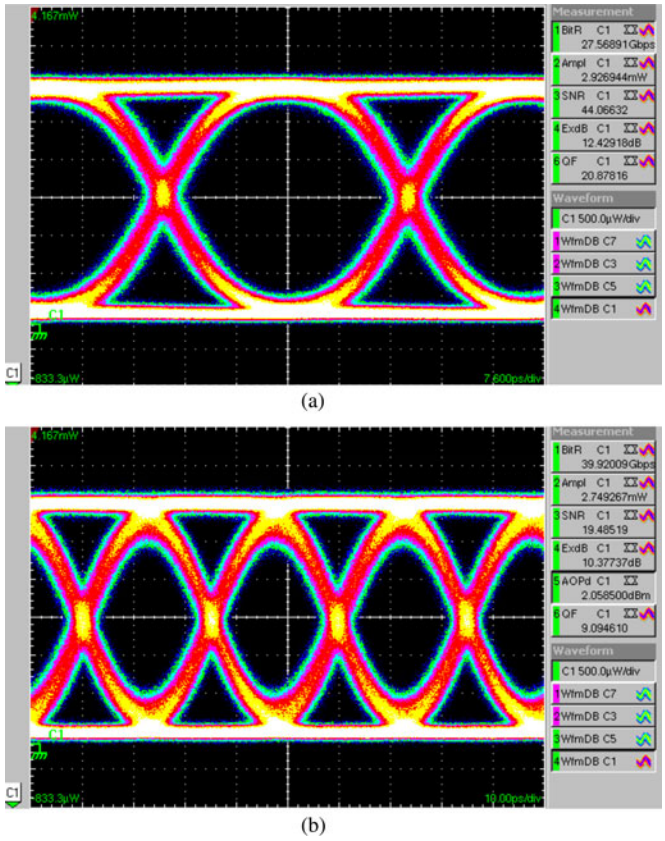

Fig. 9. Si TWMZ extinction measurement: (a) 12.4 dB extinction at 28 Gb/s and (b) 10 dB extinction at 40 Gb/s.

We measured the conversion gain of the receiver under various power levels and recorded the average power into the receiver in the each experiment. Based on these measurements, we calculated that ER is 6–7 dB in the measurement of Lithium Niobate modulator and in the measurement of silicon TWMZ modulator with 4.8 V_{pp} drive. The low ER (6–7 dB) is likely caused by the gain compression of the EDFA and photo-receiver used in the experiments. A separate measurement using a DC-coupled optical module in the DCA and without the EDFA yielded approximately 10 dB ER at 40 Gb/s (see Fig. 9). The ER is approximately 4 dB in the measurement of silicon TWMZ modulator with 1.6 V_{pp} drive. As the results in Fig. 7(b) suggest, the silicon TWMZ shows negligible OSNR penalty compared to Lithium Niobate modulator when driven with 4.8 V_{pp}. This establishes that the level of nonlinear distortion found within our silicon TWMZ is minimal and should not be an issue for utilization in communications systems [26]. The silicon TWMZ shows approximately 2 dB OSNR-penalty when driven with 1.6 V_{pp}. compared to the 4.8 V_{pp} drive and Lithium Niobate. Error-free (BER $<$ 1e-12) eye diagrams of the Lithium Niobate modulator and the silicon TWMZ modulator under different driving voltages are shown in Fig. 8.

IV. Conclusion

We demonstrate slow-wave electrode based design as a viable approach for realizing high-speed silicon traveling-wave

modulators. As more advanced low $V_\pi L$ junctions are employed in silicon modulators, slow-wave electrodes offer a promising way to drive such highly capacitive junctions at 50 Ω. We experimented periodical phase matching and showed that the EO 3-dB bandwidth closely tracked RF 6.4-dB bandwidth, indicating the RF and optical velocities overall are well matched despite their strong intrinsic mismatch within each individual section. RF cross-talk issue is addressed in our design. Single-RF-mode operation is achieved and the two device arms are fully independent, making the device compatible with differential signaling and uncorrelated signaling on the two device arms typically used in advanced modulation formats, such as QPSK. The device achieves full extinction with 5.5 V voltage on each arm and shows an EO bandwidth of 27 GHz under 1 V reverse bias. At 40 Gb/s, when driving the device with 4.8 V_{pp} on each arm, the BER versus OSNR performance of the device is comparable to that of a commercial 40 Gb/s Lithium Niobate modulator with 5.4 V_{pp} single-drive.

ACKNOWLEDGMENT

The authors would like to thank for the loan of critical equipment for this project from AT&T. They would also like to thank G. Pomrenke, of the Air Force Office of Scientific Research, for his support of the Optoelectronic Systems in Silicon effort.

REFERENCES

[1] G. T. Reed, G. Mashanovich, F. Gardes, and D. Thomson, "Silicon optical modulators," *Nature Photon.*, vol. 4, no. 8, pp. 518–526, 2010.

[2] B. Analui, D. Guckenberger, D. Kucharski, and A. Narasimha, "A fully integrated 20-Gb/s optoelectronic transceiver implemented in a standard 0.13-μm CMOS SOI Technology," *IEEE J. Solid-State Circuits*, vol. 41, no. 12, pp. 2945–2955, Dec.2006.

[3] J. Ding, H. Chen, L. Yang, L. Zhang, R. Ji, Y. Tian, W. Zhu, Y. Lu, P. Zhou, R. Min *et al.*, "Ultra-low-power carrier-depletion Mach–Zehnder silicon optical modulator," *Opt. Exp.*, vol. 20, no. 7, pp. 7081–7087, 2012.

[4] T. Baehr-Jones, R. Ding, Y. Liu, A. Ayazi, T. Pinguet, N. C. Harris, M. Streshinsky, P. Lee, Y. Zhang, A. E.-J. Lim *et al.*, "Ultralow drive voltage silicon traveling-wave modulator," *Opt. Exp.*, vol. 20, no. 11, pp. 12014–12020, 2012.

[5] X. Xiao, H. Xu, X. Li, Z. Li, T. Chu, Y. Yu, and J. Yu, "High-speed, low-loss silicon Mach–Zehnder modulators with doping optimization," *Opt. Exp.*, vol. 21, no. 4, pp. 4116–4125, 2013.

[6] M. Streshinsky, R. Ding, Y. Liu, A. Novack, Y. Yang, Y. Ma, X. Tu, E. K. S.Chee, A. E.-J. Lim, P. G.-Q. Lo *et al.*, "Low power 50 Gb/s silicon traveling wave Mach–Zehnder modulator near 1300 nm," *Opt. Exp.*, vol. 21, no. 25, pp. 30350–30357, 2013.

[7] S. Lin, and S.-Y. Wang, "High-throughput GaAs PIN electrooptic modulator with a 3-dB bandwidth of 9.6 GHz at 1.3 μm," *Appl. Opt.*, vol. 26, no. 9, pp. 1696–1700, 1987.

[8] H. Yu and W. Bogaerts, "An equivalent circuit model of the traveling wave electrode for carrier-depletion-based silicon optical modulators," *J. Lightw. Technol.*, vol. 30, no. 11, pp. 1602–1609, Jun. 2012.

[9] J. Rosenberg, W. Green, S. Assefa, D. Gill, T. Barwicz, M. Yang, S. Shank, and Y. Vlasov, "A 25 Gbps silicon microring modulator based on an interleaved junction," *Opt. Exp.*, vol. 20, no. 24, pp. 26411–26423, 2012.

[10] Y. Liu, S. Dunham, T. Baehr-Jones, A. E.-J. Lim, G.-Q. Lo, and M. Hochberg, "Ultra-responsive phase shifters for depletion mode silicon modulators," *J. Lightw. Technol.*, vol. 31, no. 23, pp. 3787–3793, Dec. 2013.

[11] F. Merget, S. S.Azadeh, J. Mueller, B. Shen, M. P.Nezhad, J. Hauck, and J. Witzens, "Silicon photonics plasma-modulators with advanced transmission line design," *Opt. Exp.*, vol. 21, no. 17, pp. 19593–19607, 2013.

[12] F. Gardes, D. Thomson, N. Emerson, and G. Reed, "40 Gb/s silicon photonics modulator for TE and TM polarisations," *Opt. Exp.*, vol. 19, no. 12, pp. 11804–11814, 2011.

[13] M. Ziebell, D. Marris-Morini, G. Rasigade, J.-M. Fédéli, P. Crozat, E. Cassan, D. Bouville, and L. Vivien, "40 Gbit/s low-loss silicon optical modulator based on a pipin diode," *Opt. Exp.*, vol. 20, no. 10, pp. 10591–10596, 2012.

[14] X. Tu, T.-Y. Liow, J. Song, X. Luo, Q. Fang, M. Yu, and G.-Q. Lo, " 50-Gb/s silicon optical modulator with traveling-wave electrodes," *Opt. Exp.*, vol. 21, no. 10, pp. 12776–12782, 2013.

[15] R. Spickermann and N. Dagli, "Experimental analysis of millimeter wave coplanar waveguide slow wave structures on GaAs," *IEEE Trans. Microw. Theory Techn.*, vol. 42, no. 10, pp. 1918–1924, Oct. 1994.

[16] J. Shin, S. R. Sakamoto, and N. Dagli, "Conductor loss of capacitively loaded slow wave electrodes for high-speed photonic devices," *J. Lightw. Technol.*, vol. 29, no. 1, pp. 48–52, Jan. 2011.

[17] L. Chen, C. R . Doerr, P. Dong, and Y.-K. Chen, "Monolithic silicon chip with 10 modulator channels at 25 Gbps and 100-GHz spacing," *Opt. Exp.*, vol. 19, no. 26, pp. B946–B951, 2011.

[18] J.-M. Liu, *Photonic Devices*, vol. 58, Cambridge, U.K.: Cambridge Univ. Press, 2005.

[19] J. Ding, H. Chen, L. Yang, L. Zhang, R. Ji, Y. Tian, W. Zhu, Y. Lu, P. Zhou, and R. Min. (2012, Jan.). Low-voltage, high-extinction-ratio, Mach–Zehnder silicon optical modulator for CMOS-compatible integration. Opt. Exp. [Online]. *20(3)*, pp. 3209–3218. Available: http://www.opticsexpress.org/abstract.cfm?URI=oe-20-3-3209

[20] M. Hochberg, N. C.Harris, R. Ding, Y. Zhang, A. Novack, Z. Xuan, and T. Baehr-Jones, "Silicon photonics: The next fabless semiconductor industry," *IEEE Solid-State Circuits Mag.,* vol. 5, no. 1, pp. 48–58, Mar. 2013.

[21] A. Novack, Y. Liu, R. Ding, M. Gould, T. Baehr-Jones, Q. Li, Y. Yang, Y. Ma, Y. Zhang, K. Padmaraju *et al.*, "A 30 GHz silicon photonic platform," in *Proc. SPIE Integr. Opt., Phys. Simul.*, vol. 8781, 878107, 2013.

[22] G. E. Ponchak, J. Papapolymerou, and M. M. Tentzeris, "Excitation of coupled slotline mode in finite-ground CPW with unequal ground-plane widths," *IEEE Trans. Microw. Theory. Techn.*, vol. 53, no. 2, pp. 713–717, Feb.2005.

[23] R. Spickermann, S. Sakamoto, and N. Dagli, "In traveling wave modulators which velocity to match?" in *Proc. IEEE Lasers Electro-Opt. Soc. Annu. Meeting,* 1996, vol. 2, pp. 97–98.

[24] R. Ding, Y. Liu, Q. Li, Y. Yang, Y. Ma, K. Padmaraju, A. E.-J. Lim, G.-Q. Lo, K. Bergman, T. Baehr-Jones *et al.*, "Design and characterization of a 30-GHz bandwidth low-power silicon traveling-wave modulator," *Opt. Commun.*, vol. 321, pp. 124–133, 2014.

[25] Y. Liu, R. Ding, Q. Li, X. Zhe, Y. Li, Y. Yang, A. E. Lim, P. G.-Q. Lo, K. Bergman, T. Baehr-Jones *et al.*, "Ultra-compact 320 Gb/s and 160 Gb/s WDM transmitters based on silicon microrings," presented at the Opt. Fiber Commun. Conf., San Francisco, CA, USA, 2014, Paper Th4G.6.

[26] M. Streshinsky, A. Ayazi, Z. Xuan, A. E.-J. Lim, G.-Q. Lo, T. Baehr-Jones, and M. Hochberg, "Highly linear silicon traveling wave Mach–Zehnder carrier depletion modulator based on differential drive," *Opt. Exp.*, vol. 21, no. 3, pp. 3818–3825, 2013.

Ran Ding received the B.S. degree in acoustics from the Department of Electronic Engineering, Nanjing University, Nanjing, China, in 2009, and the Ph.D. degree in electrical engineering from the University of Washington, Seattle, WA, USA, in March 2014. His research interests include areas of high-speed optical modulators, transceivers, and other photonics systems, as well as high-speed electronic integrated circuits for optical data communications, such as optical receiver circuits and codesigned modulator drivers.

Yang Liu received the B.S. degree in physics from Peking University, Beijing, China, and the M.S. degree in electrical engineering from the University of Washington, Seattle, WA, USA. He is currently working toward the Ph.D. degree with the Nanophotonics Group, University of Delaware, Newark, DE, USA. His current research interests include the modeling and design of integrated optical communication systems in the SOI platform.

Yangjin Ma received the B.S. degree in applied physics from Tianjin University, Tianjin, China, in 2009, and the M.S. degree in condensed matter physics from Shanghai Jiao Tong University, Shanghai, China, in 2011. He is currently working toward the Ph.D. degree in electrical and computer engineering with the University of Delaware, Newark, DE , USA, with research focus in silicon photonics. His work involves designing both novel passive silicon photonic devices and active devices toward a system-level integration.

Yisu Yang received the B.S. and M.S. degrees from the Beijing University of Posts and Telecommunications, Beijing, China, in 2007 and 2010, respectively. From 2010 to 2011, he was with Ericsson Communications Co. Ltd., Beijing, as an Optical Network Engineer. Since 2012, he has been working toward the Ph.D. degree in electronic engineering with the University of Delaware, Newark, DE, USA. His research interest includes silicon photonics application.

Qi Li received the B.Eng. degree in electrical and computer engineering with a minor in mathematics from The Hong Kong University of Science and Technology, Clear Water Bay, Hong Kong, in 2010, and the M.S. degree from Columbia University, New York, NY, USA, in 2012, where he is currently working toward the Ph.D. degree with the Department of Electrical Engineering. He spent the Spring of 2009 as an Exchange Student at Cornell University. His research interests include silicon photonics and optical interconnection networks.

Andy Eu-Jin Lim received the B. Eng. (Hons.) and Ph.D. degrees in electrical engineering from the Department of Electrical and Computer Engineering, National University of Singapore (NUS), Singapore, in 2004 and 2009, respectively. At NUS, he researched on advanced gate stacks, in particular metal gates and high-kψ dielectrics for CMOS technology. He is currently a Research Scientist with the Institute of Microelectronics, Agency for Science, Technology and Research (A*STAR), Singapore. His research interests include device physics and process integration for silicon photonics, as well as germanium-on-silicon epitaxial thin-film technology for photonics applications. Dr. Lim received the A*STAR Graduate Scholarship Award in 2004.

Guo-Qiang Lo (S'86–M'92) received the M.S. and Ph.D. degrees in electrical and computer engineering from the University of Texas at Austin, Austin, TX, USA, in 1989 and 1992, respectively. He was with the Integrated Device Technology, Inc., both in San Jose, CA, USA, and Hillsboro, OR, USA, where he was involved in Si semiconductor manufacturing areas in process and integration module research and development. Since 2004, he has been with the Institute of Microelectronics, Agency for Science, Technology and Research, Singapore, where he is the Program Director of the Nanoelectronics and Photonics Program. His current research interests include novel semiconductor device and integration technology, particularly in nanoelectronics devices and Si-microphotonics. He has authored or coauthored more than 100 peer-reviewed journal and conferences publications, and holds more than 20 granted patents. He received the IEEE George E. Smith Award for the best paper published in the IEEE ELECTRONIC DEVICE LETTERS in 2007, and National and President Technology Awards of Singapore in 2008 and 2010.

Keren Bergman (F'09) received the Ph.D. degree from the Massachusetts Institute of Technology, Cambridge, MA, USA. She is currently the Charles Batchelor Professor and the Chair of Electrical Engineering at Columbia University, New York, NY, USA, where she also directs the Lightwave Research Laboratory. She leads multiple research programs on optical interconnection networks for advanced computing systems, data centers, optical packet switched routers, and chip scale nanophotonic networks. She is a Fellow of the Optical Society of America.

Tom Baehr-Jones received the B.S. degree in physics, and the M.S. and Ph.D. degrees in applied physics, all from the California Institute of Technology (Caltech), Pasadena, CA, USA, in 2002, 2005, and 2006, respectively. He is currently a Research Associate Professor in the Nanophotonics Laboratory at the University of Delaware, Newark, DE, USA. His research interests include computational physics, integrated optics, and silicon-photonics systems. He was a Cofounder at both Simulant and Luxtera during his time as an undergraduate at Caltech. He is also the Associate Director of the Optoelectronic Systems in Silicon foundry service.

Michael Hochberg received the B.S. degree in physics, and the M.S. and Ph.D. degrees in applied physics all from the California Institute of Technology (Caltech), Pasadena, CA, USA, in 2002, 2005, and 2006, respectively. He is currently an Associate Professor of electrical and computer engineering, materials science and engineering, and chemical and biomolecular engineering at the University of Delaware, Newark, DE, USA, and has joined the Faculty in a joint position at the National University of Singapore, with an attachment at the Institute for Microelectronics, A*Star, Singapore. He currently directs the Optoelectronic Systems in Silicon effort at the University of Delaware. He received the Demetriades-Tsafka dissertation Prize in Nanotechnology as well as a National Science Foundation Graduate Research Fellowship. As an undergraduate, he received a merit-based Fellowship from Caltech and he cofounded two companies: Simulant and Luxtera. In 2007, he joined the Faculty at the University of Washington, where he received an Air Force Office of Scientific Research Young Investigators Program award, as well as a 2009 Presidential Early Career Award in Science and Engineering. His work has been funded by Intel, Air Force Office of Scientific Research, Defense Advanced Research Projects Agency, National Science Foundation , and Mentor Graphics, as well as numerous other companies and government agencies. His lab groups at UD and NUS have now produced multiple early-stage spinoff companies.